Revision 2, Word Count: 10812

3D crystal size distributions of pyroxene nanolites from nano X-ray computed tomography: Improved correction of crystal size distributions from *CSDCorrections* for magma ascent dynamics in conduits

Shota Okumura[1,*], Mayumi Mujin[2], Akira Tsuchiyama[3,4], and Akira Miyake[1]

Affiliations:

[1]Department of Geology and Mineralogy, Graduate School of Science, Kyoto University, Kitashirakawaoiwake-cho, Sakyo-ku, Kyoto 606-8502, Japan

[2]Department of Earth Science, Graduate School of Science, Tohoku University, 6-3, Aramaki-Aza-Aoba, Aobaku, Sendai 980-8578, Japan

[3]Research Organization of Science and Technology, Ritsumeikan University, 1-1-1 Nojihigashi, Kusatsu, Shiga 525-8577, Japan

[4]CAS Key Laboratory of Mineralogy and Metallogeny/Guangdong Provincial Key Laboratory of Mineral Physics and Materials, Guangzhou Institute of Geochemistry, Chinese Academy of Sciences, 511 Kehua Street, Wushan, Tianhe District, Guangzhou 510640, China

ABSTRACT

Groundmass crystals indicate syneruptive magmatic conditions, and thus their crystal size distributions (CSDs) are used to infer magma ascent histories. Three-dimensional (3D) CSDs are most commonly estimated from two-dimensional (2D) observations and plotted against long-axis length, *L* (hereafter referred to as "*L*-plot CSDs"). However, *L*-plot CSDs have two significant problems: the error owing to the conversion from 2D to 3D and a lowered sensitivity to changes in the degree of effective undercooling (ΔT_{eff}), which arises because a crystal's growth rate varies with ΔT_{eff} most strongly along its long dimension. Although these problems can result in false interpretations of magma ascent dynamics, there has been little discussion of the influence of the size criteria on CSDs.

In this study, we investigated which 3D size criterion (i.e., long (*L*), intermediate (*I*), or short (*S*) axis length) is optimum for 2D-estimated CSDs of groundmass crystals from two perspectives: (1) conformity with the actual distributions, and (2) the sensitivity of CSD slopes to the magma ascent conditions in the conduit. We observed groundmass pyroxene crystals in pumice clasts from sub-Plinian and Vulcanian eruptive phases during the 2011 eruption of Shinmoedake (andesitic volcano, Japan) by using synchrotron

radiation-based X-ray computed nanotomography (SR-XCT) and field-emission scanning electron microscopy (FE-SEM), and reinvestigated the crystallization kinetics of pyroxene nanolites ranging in width from a few hundred nanometers to 1 μm. The SR-XCT observations provided the detailed 3D shapes and 3D CSDs (CT-CSDs) of these nanolites directly. The FE-SEM observations allowed us to estimate 3D aspect ratios ($S : I : L$) and CSDs (SEM-CSDs). *L*-plot SEM-CSDs, acquired using the program *CSDCorrections*, were used to calculate *S*-plot SEM-CSDs and *I*-plot SEM-CSDs. We compared the data from FE-SEM with those from SR-XCT to evaluate the accuracy of 3D aspect ratios and CSDs estimated from 2D data.

The *L*-plot SEM-CSDs from the sub-Plinian pumice sample showed significant inconsistencies with the CT-CSD, a result of the difficulty in estimating representative 3D aspect ratios from 2D observations for fairly elongated groundmass crystals. In contrast, the *S*- and *I*-plot SEM-CSDs kept the effect of aspect ratio to a minimum and preserved their actual slopes, except for a vertical discrepancy between the CSDs. Moreover, the slopes of *S*- and *I*-plot CSDs of the nanolites differed more markedly between the two eruptive styles (by ~20% more) than those of *L*-plot CSDs. For estimating magma ascent dynamics, we

propose that the optimum method for acquiring SEM-CSDs is to measure the cross-sectional widths of crystals and convert the resulting 2D dataset into *S*-plot CSDs.

Our new finding that the 3D shapes and CSDs of pyroxene nanolites differ according to eruptive style means that nanolites indicate distinct differences in ascent histories at the shallow conduit: increasing ΔT_{eff} just before sub-Plinian eruptions and decreasing ΔT_{eff} before Vulcanian eruptions. Given the similarity in CSDs of microlites, our results suggest that eruptive style was determined in the shallow conduit. Monitoring the condition of the shallow conduit may contribute to predicting the time evolution of eruptive activity.

Keywords: Crystal size distribution, Morphology, Nanolite, X-ray computed tomography, Pyroxene, Magma ascent

INTRODUCTION

Eruptive phenomena are controlled by the conditions of magma ascent through the conduit (e.g., Cassidy et al. 2018). Recent studies have argued that the subaerial explosivity of volcanic eruptions can be determined by conditions in shallow conduits (e.g., Wadsworth et al. 2020). Magma ascent histories are thus important for understanding how eruptive styles change in conduits, and these histories are recorded by groundmass crystals, which crystallize mainly as a result of decompression-induced dehydration (e.g., Cashman and Blundy 2000). In particular, nanolites, crystals smaller than 1 μm in width (Mujin et al. 2017), are considered to reflect magmatic conditions in the shallow conduit (Mujin and Nakamura 2014). Furthermore, the presence of nanolites can affect eruptive styles by increasing magma viscosity and enhancing bubble nucleation (e.g., Di Genova et al. 2017, 2020; Hajimirza et al. 2021). The crystallization kinetics of nanolites are reflected in crystal size distributions (CSDs; Cashman and Marsh 1988; Marsh 1988); therefore, CSD analyses enable us to investigate the histories of magma ascent in conduits (e.g., Armienti et al. 1994; Marsh 1998; Mujin and Nakamura 2014).

CSDs are generally expressed as the natural logarithm of crystal population density (mm^{-4}, the number of crystals in a given size interval per unit volume) as a function of crystal size, and their slopes allow the estimation of crystallization kinetics and magma ascent dynamics (Marsh 1988, 1998). If an open system where nucleation and growth rates are fixed is considered, CSDs are used to quantify growth rates or magma residence times (Marsh 1988). However, the syneruptive ascent of magma in the conduit involves changes in nucleation and growth rates over time. In such a closed non-steady system, CSD slopes reflect the balance between nucleation and growth rates (Marsh 1998). According to Marsh (1998), log-linear CSDs generally represent an exponential increase in nucleation rate with time under steady growth, and an increase of the nucleation exponent steepens the slope of the CSD. Therefore, a CSD with a break in slope probably indicates a change in crystallization conditions, such as a magmatic event involving a drastic change in the degree of effective undercooling (ΔT_{eff}), which responds to decompression-induced dehydration.

Although CSDs are based on three-dimensional (3D) quantities, they are most often estimated from two-dimensional (2D) observations using stereological corrections (Fig. 1). Since its development, the program *CSDCorrections* (Higgins 2000) has been used to calculate almost all reported CSDs. *CSDCorrections* yields stereologically corrected CSDs from datasets of crystal cross-sectional width (w) or length (l), the area analyzed, a representative 3D crystal shape, and fabric (crystal orientation). The stereological corrections are based on the principle that w and l tend to be close to the lengths of the 3D short (S) and intermediate (I) axes, respectively, when there is no dominant lineation or foliation (Higgins 1994). Assuming that all crystals are similarly shaped in terms of their 3D aspect ratios $S : I : L$, the program converts the scale of size intervals from w or l into

DOI: https://doi.org/10.2138/am-2022-8039. http://www.minsocam.org/

the 3D long-axis length (L) as (Equation 6 in Higgins 2000):

$$L = w \times A \tag{1a}$$

$$L = l \times B \tag{1b}$$

where the constants A and B are L/S and L/I ratios for a representative 3D crystal shape, respectively. The representative 3D aspect ratio $S : I : L$ used for the corrections is also estimated from a histogram of the w/l ratios of crystal cross sections obtained from 2D observations (Higgins 1994; Morgan and Jerram 2006). Because *CSDCorrections* converts cross-sectional size data into L, most reported CSDs are expressed as a function of L (hereafter referred to as “L-plot CSDs”), except in a few recent studies (Taddeucci et al. 2004; Mujin and Nakamura 2014) and in those published before 2000 (e.g., Cashman and Marsh 1988; Armienti et al. 1994). However, the use of L as the representative size for CSDs may not be optimal; its use may stem from the fact that stereological corrections applied to non-spherical shapes are based on the diameter of a sphere circumscribed about a crystal (i.e., its maximum length; e.g., Peterson 1996).

Although CSDs were originally used to estimate crystal residence times or growth rates during static (near equilibrium) processes in steady open systems such as magma stagnation (e.g., Marsh 1988; Cashman and Marsh 1988; Hammer et al. 1999; Witter et al.

2016), they have been increasingly used to infer conditions during the syneruptive ascent of magma (e.g., Castro and Gardner 2008; Preece et al. 2013; Mujin et al. 2017; Suzuki et al. 2018). Because such non-steady closed systems should yield variable ΔT_{eff}, CSD analyses to infer syneruptive ascent dynamics must take into consideration the anisotropic kinetics of crystal growth. In this context, *L*-plot CSDs have two significant problems: (1) errors owing to the conversion from 2D to 3D and (2) relatively low sensitivity to changes in ΔT_{eff}.

(1) The 2D to 3D conversion in *CSDCorrections* derives *L* from *w* or *l* on the assumption that all crystals have the same 3D aspect ratio (Fig. 1). However, Castro et al. (2003) has shown that the aspect ratios of groundmass crystals may vary greatly and yield inaccurate *L*-plot CSDs from 2D observations. In addition, it is inherently difficult to estimate representative 3D aspect ratios of groundmass crystals from 2D data because of their elongated shapes (Morgan and Jerram 2006), and errors in the aspect ratio can significantly distort the resultant CSD (Muir et al. 2012). However, if CSDs can be obtained as a function of *S* or *I* (i.e., *S*-plot or *I*-plot CSDs) without the conversion into *L* via Equations 1, the error related to aspect ratios should be reduced (see Appendix 1).

(2) Because rock-forming minerals tend to be elongated with increasing ΔT_{eff} (e.g.,

Kouchi et al. 1983; Hammer and Rutherford 2002; Shea and Hammer 2013), the long dimension L of a crystal should be considered as the direction in which its growth rate varies most significantly with ΔT_{eff}. With increasing ΔT_{eff}, the slope of CSDs is steepened by an accelerated increase in nucleation rate (Marsh 1998); however, the increase in growth rate, which makes the slope gentler, can offset this effect (Fig. 2). Figure 2 shows simulated CSDs based on the equations in Marsh (1998) (see Appendix 2). Marsh (1998) formulated crystal population densities (*N*) with the assumption that nucleation (*J*) and growth rates (*G*) are exponential functions of time as (Equations 7, 8, and 23 in Marsh 1998):

$$J = J_o \exp(ax) \quad (2)$$

$$G = G_o \exp(bx) \quad (3)$$

$$\ln\left[\frac{N(x)}{N_o}\right] = \ln[1 - \varphi(x)] + (a - b)x \quad (4)$$

where a and b are constants, φ is the crystal fraction, x is dimensionless time (0–1), and the subscript o for the parameters indicates the initial values (i.e., at time x = 0). The slope of CSD is approximately given by $(a - b)/L_m$, where L_m is the maximum crystal size. When the growth rate is nearly constant (i.e., $b \sim 0$; Fig. 2c), the slope of CSD responds primarily to the nucleation rate (i.e., a) (Marsh 1998). In contrast, because increases in growth rate and its dependence on ΔT_{eff} (i.e., G_o and b) decrease the slope of CSD, rapid crystallization associated with accelerated growth can produce a CSD resembling one resulting from slower nucleation and growth (Fig. 2d). Hence, it is possible that the slopes of *L*-plot CSDs insufficiently reflect changes in ΔT_{eff}. On the other hand, if the growth rate along the short axis (*S*) is the least affected by ΔT_{eff}, *S*-plot CSDs should reflect temporal changes in nucleation rate most clearly and be more sensitive to magma ascent conditions.

These problems in the prevalent *L*-plot CSDs can result in false interpretations of magma ascent dynamics; however, there has been little discussion of the influence of size criteria on CSDs. Instead of *L* plots, we propose the use of *S*-plot CSDs for the investigation of magma ascent histories. *S*-plot CSDs are transformed from the *L*-plot CSDs that *CSDCorrections* calculates from 2D datasets (Fig. 1). In this study, we acquired CSDs estimated from 2D scanning electron microscope (SEM) observations (SEM-CSDs), and here we discuss their optimum representation among *L*, *I*, and *S* plots from two perspectives: (1) conformity with the actual distributions and (2) sensitivity of CSD slopes to magma ascent conditions in the conduit. Because nanolites probably reflect the difference in magma conditions among different eruptive styles most strongly (Mujin and Nakamura 2014), we focus on the kinetics of nanolites.

To obtain accurate CSDs of nanolites directly, we used synchrotron radiation–

based X-ray computed nanotomography (SR-XCT) with spatial resolutions on the order of 100 nm (e.g., Uesugi et al. 2006; Takeuchi et al. 2009; Tsuchiyama et al. 2011). These 3D observations yielded detailed 3D shapes of very small groundmass crystals (less than several μm in width) and reliable CSDs free of stereological errors (CT-CSDs) that enabled us to evaluate the accuracy of the SEM-CSDs for each size criterion.

To verify the sensitivity of CSD slopes, we analyzed pumice samples from sub-Plinian and Vulcanian eruptions during the 2011 activity of Shinmoedake, an andesitic volcano in Japan, which represent two distinct ascent histories. CSDs of plagioclase have shown that the magma ascent conditions in the shallow conduit differed between the sub-Plinian and Vulcanian eruptions (Mujin and Nakamura 2014; Mujin et al. 2017; Suzuki et al. 2018); however, the CSDs of pyroxene were similar (Mujin and Nakamura 2014; Mujin et al. 2017; note that Figure 3 of Mujin et al. 2017 displays *L*-plot CSDs). Pyroxene is an important phase that indicates magma conditions (e.g., Ubide and Kamber 2018; Arzilli et al. 2019; Masotta et al. 2020); therefore, pyroxene CSDs should reflect the same differences in ascent paths that plagioclase recorded. A possible reason for the discrepancy between plagioclase and pyroxene is the selection of samples analyzed. Mujin and Nakamura (2020) noted that the pyroclasts from the Shinmoedake 2011 eruption previously analyzed by Mujin and Nakamura (2014) and Mujin et al. (2017) are classified into two types based on their glass chemical composition and that one of the five Vulcanian pumice clasts they analyzed belonged to the same group as the sub-Plinian pumice. Because the Vulcanian pumice samples of Mujin and Nakamura (2014) and Mujin et al. (2017) included both types, we selected the characteristic pumice for each eruptive style for reanalysis in this study. Here, we reexamine whether the kinetics of pyroxene nanolites reflect the different ascent histories.

SAMPLE DESCRIPTION

We selected pumice samples from the 2011 eruption of Shinmoedake, an andesitic volcano in the Kirishima volcano group, southern Kyushu, Japan. Since this eruption included various eruptive styles, pumice samples from different phases of the eruption allowed investigation of the effects of ascent dynamics on the observed CSDs. The chronology of the 2011 Shinmoedake eruption is well documented by various observations (Kozono et al. 2013; Nakada et al. 2013; Kato and Yamasato 2013). The climactic phase of the eruption (26–31 January 2011) was characterized by three sub-Plinian eruptions and the subsequent extrusion of a lava dome within the crater, associated with intermittent

DOI: https://doi.org/10.2138/am-2022-8039. http://www.minsocam.org/

Vulcanian eruptions; this activity was followed by repeated Vulcanian eruptions and explosive events from 1 February to 13 March 2011. In this study, we examined two gray pumice clasts: one from a sub-Plinian eruption and the other from a Vulcanian explosion. These samples were collected on 24 July 2011 at Takachihogawara, 3 km south of Shinmoedake crater. The sub-Plinian pumice was collected from a well-sorted pumice fall deposit emplaced during the first and second sub-Plinian events (layers 2–4 of Nakada et al. 2013). The Vulcanian pumice was collected from the topmost surface of the pumice deposits emplaced by the three sub-Plinian eruption columns (layer 5 of Nakada et al. 2013; unit 3U of Miyabuchi et al. 2013). Although the precise explosion that produced the Vulcanian pumice has not been determined, it most likely occurred on 1 or 11 February or 13 March (Mujin et al. 2017). Nonetheless, the pumice clasts are distinct because the Vulcanian explosions produced larger pumice than the sub-Plinian eruption. Sample collection details are reported in Mujin and Nakamura (2014).

Suzuki et al. (2013) reported that the products of the sub-Plinian and Vulcanian eruptive phases are similar in bulk chemical composition (57–58 wt% SiO_2), except for white pumice (62–63 wt% SiO_2). However, interstitial glass compositions vary according to eruption style: those of Vulcanian products tend to be more evolved than those of sub-Plinian pumice, probably due to magma stagnation in the conduit preceding the Vulcanian explosions (Suzuki et al. 2018; Mujin and Nakamura 2020). Mujin and Nakamura (2020) divided the Shinmoedake pyroclasts into two groups based on the glass compositions: less silicic group 1 with SiO_2 < 71 wt% and silicic group 2 with SiO_2 > 71 wt%. The sub-Plinian pumice clasts belong to group 1, whereas four of five Vulcanian pumice clasts belong to group 2. Although the Vulcanian pumice samples of previous studies (Mujin and Nakamura 2014; Mujin et al. 2017) included some from group 1, we selected a group 2 Vulcanian pumice and a group 1 sub-Plinian pumice as representative samples of each eruptive style (Table 1). Therefore, we assume that these two pumice samples experienced distinct ascent dynamics.

Gray pumice clasts from the 2011 Shinmoedake eruption contain phenocrysts (> 100 μm) of plagioclase, clinopyroxene (Cpx), orthopyroxene (Opx), olivine, magnetite, and ilmenite, some of which show reaction rims indicating the intrusion of a higher-temperature magma (Suzuki et al. 2013). Their groundmass is charged with crystals of plagioclase, pyroxenes, and Fe-Ti oxides. Backscattered electron (BSE) images of both samples used in this study are shown in Figure 3. The pumice samples do not contain crystals smaller than 30 nm, referred to as ultrananolites (Mujin et al. 2017). This study analyzed groundmass pyroxene crystals smaller than several micrometers in width, and focused particularly on pyroxene nanolites (ranging from a few hundred nanometers to 1 μm in width) to reinvestigate their crystallization kinetics. Because they are considered to form in the shallow conduit before magma fragmentation, their kinetics should reveal magma ascent dynamics at shallow depths. As mentioned in Mujin et al. (2017), most groundmass pyroxene crystals wider than about 100 nm show parallel intergrowths of Opx and Cpx. We therefore treated them as a single pyroxene phase.

ANALYTICAL PROCEDURE

FE-SEM-EDS analyses

BSE images of polished sections of the pumice samples were obtained at an acceleration voltage of 15 kV, a 10-mm working distance, and an image resolution of ca. 25 nm/pixel using a JEOL JSM-7001F field-emission SEM (FE-SEM) at Kyoto University (Fig. 3). Quantitative compositional analyses of interstitial glasses were performed using the FE-SEM coupled with an Oxford Instruments X-Max^N 150 mm^2 energy dispersive X-ray spectrometer (EDS) and its associated analytical software *AZtec*. We analyzed 50 square regions (~1 × 1 μm) in each sample for 40 s each at an acceleration voltage of 15 kV and a beam current of about 0.3 nA. The averaged compositions of each sample are reported in Table 1.

SR-XCT observation

We acquired the 3D shapes of groundmass pyroxene crystals by SR-XCT at beamline BL47XU of the SPring-8 synchrotron facility (Hyogo, Japan; Uesugi et al. 2006; Takeuchi et al. 2009), which permits the nondestructive acquisition of 3D structures at high signal-to-noise ratios and high spatial resolution (~200 nm; e.g., Matsumoto et al. 2019). We extracted two equant microscale specimens about 20–25 μm wide from each pumice sample (sP_1 and sP_2 from the sub-Plinian pumice and Vul_1 and Vul_2 from the Vulcanian pumice; Table 2) using a FEI Quanta 200 3DS focused ion beam (FIB) system at Kyoto University (the extracted regions differed from those observed by SEM). In the FIB system, a Ga^+ ion gun was used at an acceleration voltage of 30 kV and a beam current of 0.03–65 nA. Each specimen was then mounted on a tungsten needle for SR-XCT analysis.

SR-XCT observations were performed in absorption-contrast mode using an optical imaging system with a Fresnel zone plate and the sample-to-detector distance set at ca. 7.6 m, at a single X-ray energy of 7.35 keV. This system provided a voxel size of 25–40 nm (Table 2) for an effective resolution of ~200 nm. Projection images were acquired every

0.1° during a total sample rotation of 180°, resulting in 1800 projections per specimen. The 3D CT images were reconstructed from the projection images using a convolution back-projection algorithm (Nakano et al. 2000). Details of the sample preparation and CT imaging procedures are reported in Miyake et al. (2014) and Matsumoto et al. (2019), respectively.

The obtained CT images show X-ray absorption contrasts (Fig. 4a), providing the spatial distribution of the X-ray linear attenuation coefficients of the constituent materials. The linear attenuation coefficient of an object is a function of its chemical composition and density and the X-ray energy (Koch and MacGillavry 1962; Hubbel and Seltzer 2004), and thus can be used to identify minerals and roughly estimate their chemical compositions (e.g., Tsuchiyama et al. 2012). Thus, we discriminated pyroxenes from the other minerals on the basis of pixel values (Fig. 4a). We then binarized the images with thresholds based on visual inspection, denoised the binary images by erosion and dilation by 1 pixel, and extracted the 3D data of the pyroxene crystals using the software package *Slice* (Nakano et al. 2006). Due to the low signal-to-noise ratio, CT images of specimen Vul_2 were denoised using iterative nonlocal means (Bruns et al. 2017) before binarization: this process reduced the effort involved in binarization by smoothing the inside of crystals but did not affect the quality of the extracted 3D data.

We determined the triaxial lengths (*S*, *I*, and *L*) and directions of elongation of the pyroxenes by ellipsoid fitting in *Slice* (e.g., Tsuchiyama et al. 2011). These measurements were restricted to crystals entirely contained within the specimens, effectively limiting the size range of measurable crystals to 100 nm to 20 μm in length. Pyroxene population densities were calculated from all the measured crystals for comparison with the values estimated from the SEM observations, whereas 3D aspect ratios were not calculated for crystals smaller than 5 pixels wide because of the low reliability of shapes comprising such few pixels.

Acquisition of crystal size distributions

CSDs from SR-XCT (CT-CSDs). The triaxial lengths of the crystals measured by SR-XCT yielded CSDs as a function of *S*, *I*, or *L*. CSDs are plotted based on logarithmic size intervals with five intervals per decade above 100 nm (i.e., each interval is $10^{0.2}$ times as large as the next smaller interval: $10^{2.0}$–$10^{2.2}$ nm, $10^{2.2}$–$10^{2.4}$ nm, $10^{2.4}$–$10^{2.6}$ nm …). The number of crystals in each interval was counted and divided by the volume of the CT specimens, excluding vesicles. If the number of crystals counted within an interval was less than three, the data in that interval were excluded. Then, the number density per unit volume in each interval was divided by the interval width to obtain population density (*N*), and ln(*N*) was plotted against crystal size interval. Counting errors are taken as the square root of the number of crystals within an interval.

CSDs from FE-SEM images (SEM-CSDs). The program *CSDslice* (Morgan and Jerram 2006) estimates a representative 3D aspect ratio of crystals in a sample from 2D data. Most recent CSD analyses have used some combination of *CSDslice* and *CSDCorrections* (e.g., Jerram et al. 2009; Brugger and Hammer 2010; Preece et al. 2013; Witter et al. 2016; Mujin et al. 2017; Suzuki et al. 2018). Assuming that all the observed crystals have similar 2D shapes and no preferred orientation, *CSDslice* compares the histogram of observed cross-sectional aspect ratios (i.e., *w*/*l*) to a database comprising *w*/*l* histograms for 703 different 3D aspect ratios, and estimates the most plausible shape on the basis of least-squares fitting.

In the present study, we analyzed square regions with side lengths of about 0.2 mm in both the sub-Plinian and Vulcanian pumice samples. We made mosaic images of the analyzed regions from the multiple BSE images obtained by FE-SEM (ca. 25 nm per pixel). Using *ImageJ* software, we measured the area of the sample examined (groundmass crystals and glass, but excluding vesicles) and the widths (*w*), lengths (*l*), and angles of the best-fit ellipses to the cross sections of pyroxene crystals. We then obtained *L*-plot SEM-CSDs from the datasets of cross-sectional sizes (*w*, *l*) using *CSDCorrections* version 1.6 (Table 3). As with the CT-CSDs, if the number of counted cross sections within a size interval was less than three, the data in that interval were excluded. For the stereological conversions, we used estimated values from the 2D data obtained using *CSDslice* (S'_{2D} : I'_{2D} : L'_{2D}, where ′ denotes estimated values). In addition, the SEM-CSDs corrected with the XCT average values instead of the estimates are also considered in the discussion and implications sections and Appendix 3. We refer to SEM-CSDs converted from *w* datasets as SEM(*w*)-CSDs, and those converted from *l* as SEM(*l*)-CSDs.

After using *CSDCorrections* to obtain *L*-plot SEM(*w*)-CSDs and SEM(*l*)-CSDs, we converted them into *S*-plot SEM(*w*)-CSDs and *I*-plot SEM(*l*)-CSDs, respectively. This procedure avoids the shape correction on the size scale in Equation 1. For this reason, fewer stereological corrections are required to produce *S*- and *I*-plot CSDs than *L*-plot CSDs (see Appendix 1). These conversions are expressed as:

$$S_i = L_i/A \quad (5a)$$

$$I_i = L_i/B \quad (5b)$$

$$\ln N_i(S) = \ln N_i(L) + \ln A \quad (6a)$$

$$\ln N_i(I) = \ln N_i(L) + \ln B \quad (6b)$$

where the constants A and B are L'_{2D}/S'_{2D} and L'_{2D}/I'_{2D} ratios, respectively, and N_i is the population density in the ith size interval and the plot type is indicated in parentheses. In Equations 5, S_i, I_i, and L_i are the center of the ith size interval for each plot type. We obtained S-plot CSDs by plotting $\ln N_i(S)$ against S_i, and the same applies to I-plot CSDs.

We thus obtained seven types of CSDs: S-plot CT-CSDs and SEM(w)-CSDs, I-plot CT-CSDs and SEM(l)-CSDs, and L-plot CT-CSDs, SEM(w)-CSDs, and SEM(l)-CSDs. L-plot SEM(w)-CSDs and L-plot SEM(l)-CSDs are the most prevalent in the literature.

RESULTS

CT-CSDs

We analyzed the 3D shapes of groundmass pyroxene crystals 0.1 μm to several micrometers wide and shorter than 20 μm. Figure 4a shows representative individual CT images of each specimen and Figure 5 shows 3D reconstructions of the groundmass pyroxenes. Pyroxene crystals are acicular (Fig. 5) and appear to be aligned along a plane, especially in specimens sP_1 and sP_2 (Fig. 4b), although they do not form any obvious lineation. This apparent alignment arises from the presence of large tabular plagioclase

This is the peer-reviewed, final accepted version for American Mineralogist, published by the Mineralogical Society of America.
The published version is subject to change. Cite as Authors (Year) Title. American Mineralogist, in press.
DOI: https://doi.org/10.2138/am-2022-8039. http://www.minsocam.org/

microlites (>10 μm; Fig. 4a): acicular pyroxene crystals near those plagioclases are aligned along their faces. Pyroxene morphologies differ according to eruption style (Fig. 5): pyroxenes in the sub-Plinian pumice are elongate prisms with swallowtail textures (Fig. 5b), whereas those in the Vulcanian pumice are slightly thicker prisms with flat ends (Fig. 5d). The 3D aspect ratios of the pyroxenes varied considerably in both pumice samples (Fig. 6a). Figure 6b shows the relationship between the short-axis length (S) and the degree of elongation (L/S) of the pyroxenes. Of the smaller pyroxenes (S < 600 nm), some are significantly elongated (L/S > 20), especially in the sub-Plinian pumice. However, this tendency may result from the limited volume of the CT specimens (ca. 20–25 μm on a side) because some longer crystals may have been truncated and thus excluded from our analysis. Indeed, the distributions in Figure 6b are restricted to within the L = 20 μm contour, which corresponds to the size of the CT specimens. Figure 5 shows the distributions of pyroxene aspect ratios (L/S) in each pumice. The average 3D aspect ratio was higher in the sub-Plinian (1.0 : 1.4 : 9.4) than in the Vulcanian pumice (1.0 : 1.3 : 5.1; Table 4).

Figure 8 shows CT-CSDs measured directly in 3D as functions of S, I, and L. The CT-CSDs show log-linear trends with downturns at small sizes (S, I < 0.5 μm; L < 3 μm), although the Vulcanian L-plot CSD shows an exceptional increase in the smallest size

DOI: https://doi.org/10.2138/am-2022-8039. http://www.minsocam.org/

fraction (Fig. 8c). Because these downturns occur at sizes larger than the minimum size at which crystals can clearly be distinguished in the images (0.2 μm), they are likely true, rather than apparent. In each pumice, the slopes of the CSDs become steeper from *L*- to *I*- to *S*-plot CSDs (Table 4). The slopes of the CSDs are consistently steeper in the sub-Plinian than in the Vulcanian pumice, but this difference is markedly less distinct in the *L*-plot CSDs (Fig. 8). The number density of pyroxenes per unit volume was higher in the sub-Plinian (7.62×10^6 mm^{-3}) than in the Vulcanian pumice (5.75×10^6 mm^{-3}; Table 4).

SEM-CSDs

We estimated the representative 3D aspect ratios of groundmass pyroxenes in each pumice from the histograms of their *w*/*l* ratios using *CSDslice*. Figure 9 compares the normalized histogram of *w*/*l* measured by SEM with those simulated by *CSDslice*. Compared to the *w*/*l* histograms simulated for the crystal shape closest to the XCT average in the *CSDslice* database (1.0 : 1.4 : 9.0 for sub-Plinian, 1.0 : 1.3 : 5.0 for Vulcanian), the measured histograms in each pumice are enriched in more equant crystal cross sections (i.e., higher *w*/*l* values) and lacking in more elongated cross sections (i.e., lower *w*/*l* values). The 3D aspect ratios estimated using *CSDslice* (S'_{2D} : I'_{2D} : L'_{2D}) were 1.0 : 1.4 : 2.3 for the sub-Plinian pumice and 1.0 : 1.1 : 4.5 for the Vulcanian one (Table 4). This estimate is similar to the XCT average for the Vulcanian pumice (1.0 : 1.3 : 5.1; Fig. 7b), but markedly different for the sub-Plinian pumice (1.0 : 1.4 : 9.4; Fig. 7a).

CSDCorrections can quantitatively evaluate the degree of preferred crystal orientation as the alignment factor (where 0.00 indicates no foliation and 1.00 indicates perfectly foliated rocks) from a dataset of angles defined by the long-axis directions of their cross sections. The alignment factors of the datasets used to compile the SEM-CSDs (parameters provided in Table 3) are 0.13 and 0.06 for the sub-Plinian and Vulcanian pumice, respectively, consistent with our SR-XCT observations (Fig. 4b); we therefore conclude that there is no preferred lineation in the pumice samples.

Figure 10 shows the *S*-, *I*-, and *L*-plot SEM-CSDs of each pumice sample. Each sample exhibits concave upward curvature, as reported by Mujin et al. (2017). In addition, the slopes of the nanolite distributions are steeper for the sub-Plinian than for the Vulcanian pumice. Furthermore, the shapes of the SEM(w)-CSDs and SEM(l)-CSDs differ slightly, especially in the Vulcanian *L* plot (Fig. 10c). Unlike the other CSDs, the sub-Plinian SEM(w)-CSDs do not exhibit a downturn at very small sizes (Fig. 10a and 10c), only a roll-off. The number densities per unit volume calculated by *CSDCorrections* based on l are similar to the XCT values (Table 4), whereas those based on *w* are twice as high.

DISCUSSION

Anisotropic kinetics of crystal growth and its effect on CSDs

The degree of elongation of pyroxene nanolites is higher in the sub-Plinian than in the Vulcanian pumice (Figs. 6b and 7). Considering the similarities in their bulk chemical compositions (Suzuki et al. 2013) and microlite CSDs (Fig. 12b and Figs. S2d–f in Appendix 3; Mujin et al. 2017), there should have been little difference between the sub-Plinian and Vulcanian magmas before nanolite crystallization (Mujin and Nakamura 2020). Because rock-forming minerals tend to be more elongated with increasing ΔT (e.g., Shea and Hammer 2013), this difference in the degree of crystal elongation indicates that the sub-Plinian magma experienced greater effective undercooling during its ascent through the conduit than the Vulcanian magma. Consistently, the pyroxene nanolites in the sub-Plinian pumice show swallowtail textures (Fig. 5b) and have steeper CT-CSDs slopes than those in the Vulcanian pumice (Fig. 8; Table 4), both also suggesting a greater degree of effective undercooling. Because Shea and Hammer (2013) found that the dominant morphology of clinopyroxene was euhedral at $\Delta T < 112$ K in a hydrous basaltic-andesite

DOI: https://doi.org/10.2138/am-2022-8039. http://www.minsocam.org/

magma, the sub-Plinian magma might have experienced ΔT_{eff} > 112 K at the shallow conduit.

It is notable that the difference in the CT-CSD slopes between the pumice samples is more pronounced in the *S* and *I* plots than in the *L* plot (by ~20%; Table 4), indicating that the *L*-plot slopes are relatively insensitive to magma ascent conditions. In conjunction with the difference in the degree of crystal elongation, this result confirms our assumption that anisotropic crystal growth is an important factor in CSDs and that the prevalent *L*-plot CSDs are not the most suitable CSD for investigating magma ascent dynamics in conduits (Fig. 2).

Consistency of SEM-CSDs with CT-CSDs

Assuming that CT-CSDs reflect true CSDs, we compared the SEM-CSDs with the CT-CSDs for each plot type (Fig. 11). Although the SEM-CSDs were similar to the CT-CSDs for the Vulcanian sample, they were markedly different for the sub-Plinian one. We attributed the several discrepancies between these two types of CSDs to two main factors: (1) the fundamental nature of XCT vs. SEM observation methods, and (2) the estimation of the 3D aspect ratio to construct the SEM-CSDs. Because of the limited size of the CT specimen, the size range of the crystals measured by SR-XCT was restricted (Fig. 11). Moreover, the SR-XCT data were greatly affected by local textures in the pumice samples: population densities of the sub-Plinian CT-CSDs are likely underestimated because the large plagioclase microlites in the CT specimens (Fig. 4a) reduced the volumetric proportion of regions containing pyroxene crystals compared to the entire pumice. However, we attributed the large vertical discrepancies in the sub-Plinian CSDs (Figs. 11a and 11b) mainly to the error induced by estimating the representative 3D aspect ratio to build the SEM-CSDs. Indeed, using the actual XCT average 3D aspect ratio instead of one estimated from 2D measurements reduced the discrepancies (see Appendix 3, Fig. S2).

Despite the large gaps between them, the slopes of the SEM-CSDs were similar to those of the CT-CSDs in the *S* and *I* plots (Figs. 11a and 11b; Table 4). However, the sub-Plinian *L*-plot SEM-CSDs showed significantly steeper slopes, and were thus quite different from the CT-CSD (Fig. 11c). These results indicate that although *w* and *l* were appropriately converted to *S* and *I*, the conversion from *S* and *I* into *L* involved a large error. Accordingly, we attributed the distorted shapes of the sub-Plinian *L*-plot SEM-CSDs to the inappropriate value of the estimated 3D aspect ratio used ($S'_{2D} : I'_{2D} : L'_{2D}$). Again, using the

DOI: https://doi.org/10.2138/am-2022-8039. http://www.minsocam.org/

XCT average value produced sub-Plinian *L*-plot SEM-CSDs with similar slopes to the CT-CSD (Table 4; Appendix 3, Fig. S2).

The misestimated 3D aspect ratio in the sub-Plinian pumice (1.0 : 1.4 : 2.3; Fig. 7a) arose from the small proportion of elongated pyroxene cross sections in 2D (Fig. 9a). Although this might indicate that the crystals were preferentially oriented perpendicular to the polished sample surface, no such lineation was observed by SEM with *CSDCorrections* or by SR-XCT (Fig. 4b). Instead, this underestimation may be attributed to the nature of the 2D estimation itself. Because acicular crystals are less likely to show their elongate cross sections, an accurate 2D estimation of their 3D aspect ratio requires analyzing a larger number of cross sections. Nonetheless, our analysis of the sub-Plinian pumice (793 cross sections; Table 3) satisfied the number required for a reliable estimation of phenocrysts (>200; Morgan and Jerram 2006). Thus, this underestimation suggests that the varied and considerably elongated ($L/S > 10$) shapes of groundmass crystals make 2D estimation difficult.

Although Mujin et al. (2017) used 2D measurements to successfully estimate the 3D aspect ratios of groundmass pyroxene crystals in ejecta from the Shinmoedake 2011 eruption (e.g., $S'_{2D} : I'_{2D} : L'_{2D} = 1.0 : 1.0 : 8.0$), our results highlight the possibility that 2D estimations fail to capture the 3D shape of groundmass crystals. In that case, *L*-plot SEM-CSDs are significantly distorted by the misestimated aspect ratio, which could lead to false inferences of magma ascent histories. Importantly, *S*-plot and *I*-plot SEM-CSDs preserve the true slopes even when a misestimated 3D aspect ratio is used because fewer stereological corrections are applied to construct them (Figs. 11 and S1; Table 4; see Appendixes 1 and 3). Therefore, they represent differences in magma ascent conditions with higher reliability.

Our investigation showed that *S*-plot and *I*-plot SEM-CSDs have higher reliability and sensitivity to changes in syneruptive ascent conditions of magma than *L*-plot CSDs. Additionally, because *w* datasets yield more accurate SEM-CSDs than *l* datasets (Higgins 1994, 2000), *S* plots are probably more reliable than *I* plots. In conclusion, we recommend *S*-plot SEM(*w*)-CSDs as the optimum type of SEM-CSDs for investigations of magma ascent histories.

IMPLICATIONS

Previous studies of the Shinmoedake 2011 eruption (Mujin and Nakamura 2014; Mujin et al. 2017) have reported that the CSDs of groundmass pyroxene crystals in

Vulcanian pumice clasts were almost the same as those in sub-Plinian pumice clasts. This study has revealed instead that there are differences in the CSDs of pyroxene nanolites between the sub-Plinian and Vulcanian pumice samples (Fig. 12b). We identify two reasons for these different results. First, we disregarded Vulcanian pumice clasts that were similar to the sub-Plinian ones and selected representative pumice samples of each eruptive style. Second, we expressed the CSDs as a function of 3D short-axis length (i.e., *S*-plot CSDs). Figure 12 shows the CT-CSDs and the SEM(*w*)-CSDs that were corrected with the XCT average 3D aspect ratios instead of the 2D-estimated values. Even when the SEM-CSDs were corrected with the appropriate values of 3D aspect ratio, the *L*-plot CSDs did not show a clear difference between the eruptive styles (Fig. 12a; Table 4). In contrast, the *S*-plot CSDs allowed the crystallization kinetics of pyroxene nanolites in the two eruption styles to be clearly distinguished (Fig. 12b; Table 4). As shown in the *S*-plot CSDs of nanolites (Fig. 12b inset), the slopes are steeper in the sub-Plinian pumice, whereas gentler slopes and a larger size range of the roll-off and downturn ($S < 0.8$ μm) characterize the Vulcanian pumice. Because the slopes of *S*-plot CSDs reflect the change in nucleation rate during magma ascent, these CSDs show that the crystallization kinetics of sub-Plinian and Vulcanian pumice were nucleation-dominant and growth-dominant, respectively. These results indicate distinct ascent histories in the shallow conduit: the magma ascent rate and resultant ΔT_{eff} were increasing just before the sub-Plinian eruption and decreasing before the Vulcanian eruption. This inference is consistent with the features of crystal morphology as discussed above. Given the similarity in the distribution of microlites in the two pumice samples (Fig. 12b), the nanolite evidence suggests that the magma ascent conditions bifurcated crucially in the shallow conduit.

Kozono et al. (2013) determined from geodetic observations during the Shinmoedake 2011 eruption that the Vulcanian explosions did not involve deflation of a magma chamber. Therefore, the Vulcanian pumice clasts appear to have originated in the magma batch that had ascended during the preceding lava extrusion phase and had stagnated in the conduit until the Vulcanian explosions. For this reason, our comparison of the sub-Plinian and Vulcanian pumice samples is effectively a comparison between the explosive and effusive phases. Kozono et al. (2013) also indicated that the Shinmoedake 2011 eruption was in a critical state between explosive and effusive because the magma discharge rates for the sub-Plinian eruptions and the lava extrusion phase were near the boundary between those for historic Plinian and lava-dome eruptions of other global volcanoes. Although conditions of the magma chamber, such as overpressure, are an important factor (e.g., Jaupart and Allègre 1991; Woods and Koyaguchi 1994; Degruyter et al. 2016), our results suggest that the condition of the shallow conduit conclusively determined the eruptive explosiveness. One plausible explanation is that the shallow conduit was occluded during the period between the third sub-Plinian eruption and the lava extrusion phase. Wadsworth et al. (2020) proposed a model in which sintering of fragmented magma on the conduit wall results in occlusion of the shallowest part of the conduit and triggers the transition from explosive into effusive eruptions. This model explains the similarity in microlite CSDs between explosive and effusive products (e.g., Castro and Gardner 2008). Consistent with that proposal, Mujin and Nakamura (2020) suggested the welding of pyroclasts; additionally, a study based on the one-dimensional steady flow model (Tanaka and Hashimoto 2013) found that a narrow conduit prevented magma fragmentation (i.e., sub-Plinian eruption) in the Shinmoedake 2011 eruption. These considerations suggest that monitoring the diameter of the shallow conduit can contribute to predicting the time evolution of eruptive activity.

ACKNOWLEDGMENTS

The authors thank Kentaro Uesugi, Akihisa Takeuchi, Masahiro Yasutake, and

Tsukasa Nakano for supporting the SR-XCT experiments and Junya Matsuno for supporting the image processing. We thank the anonymous reviewer, Fabio Arzilli, and Maurizio Petrelli for many constructive comments that significantly improved our manuscript. The SR-XCT experiments at SPring-8 in this study were conducted under the proposal nos. 2018A1373, 2018B1298, 2019A0166, and 2019B0166. This work was supported by the Sasakawa Scientific Research Grant from the Japan Science Society. Funding was provided to AM by a Grant-in-Aid for Scientific Research by the Japan Society for the Promotion of Science (JP16H06348).

REFERENCES

Armienti, P., Pareschi, M.T., Innocenti, F., and Pompilio, M. (1994) Effects of magma storage and ascent on the kinetics of crystal growth. Contributions to Mineralogy and Petrology, 115, 402–414.

Arzilli, F., La Spina, G., Burton, M.R., Polacci, M., Le Gall, N., Hartley, M.E., Di Genova, D., Cai, B., Vo, N.T., Bamber, E.C., and others. (2019) Magma fragmentation in highly explosive basaltic eruptions induced by rapid crystallization. Nature Geoscience, 12, 1023–1028.

Brugger, C.R., and Hammer, J.E. (2010) Crystal size distribution analysis of plagioclase in experimentally decompressed hydrous rhyodacite magma. Earth and Planetary Science Letters, 300, 246–254.

Bruns, S., Stipp, S.L.S., and Sørensen, H.O. (2017) Looking for the signal: A guide to iterative noise and artefact removal in X-ray tomographic reconstructions of porous geomaterials. Advances in water resources, 105, 96–107.

Cashman, K., and Blundy, J. (2000) Degassing and crystallization of ascending andesite and dacite. Philosophical Transactions of the Royal Society of London A: Mathematical, Physical and Engineering Sciences, 358, 1487–1513.

Cashman, K.V., and Marsh, B.D. (1988) Crystal size distribution (CSD) in rocks and the kinetics and dynamics of crystallization II: Makaopuhi lava lake. Contributions to Mineralogy and Petrology, 99, 292–305.

Cassidy, M., Manga, M., Cashman, K., and Bachmann, O. (2018) Controls on explosive-effusive volcanic eruption styles. Nature communications, 9, 2839.

Castro, J.M., and Gardner, J.E. (2008) Did magma ascent rate control the explosive-effusive transition at the Inyo volcanic chain, California? Geology, 36, 279–282.

Castro, J.M., Cashman, K.V., and Manga, M. (2003) A technique for measuring 3D crystal-size distributions of prismatic microlites in obsidian. American Mineralogist, 88, 1230–1240.

Degruyter, W., Huber, C., Bachmann, O., Cooper, K.M., and Kent, A.J.R. (2016) Magma reservoir response to transient recharge events: The case of Santorini volcano (Greece). Geology, 44, 23–26.

Di Genova, D., Kolzenburg, S., Wiesmaier, S., Dallanave, E., Neuville, D.R., Hess, K.U., and Dingwell, D.B. (2017) A compositional tipping point governing the mobilization and eruption style of rhyolitic magma. Nature, 552, 235–238.

Di Genova, D., Brooker, R.A., Mader, H.M., Drewitt, J.W.E., Longo, A., Deubener, J., Neuville, D.R., Fanara, S., Shebanova, O., Anzellini, S., and others. (2020) In situ observation of nanolite growth in volcanic melt: A driving force for explosive eruptions. Science advances, 6, eabb0413.

Hajimirza, S., Gonnermann, H.M., and Gardner, J.E. (2021) Reconciling bubble nucleation in explosive eruptions with geospeedometers. Nature Communications, 12, 283.

Hammer, J.E., and Rutherford, M.J. (2002) An experimental study of the kinetics of decompression-induced crystallization in silicic melt. Journal of Geophysical

Research, 107, 1–23.

Hammer, J.E., Cashman, K.V., Hoblitt, R.P., and Newman, S. (1999) Degassing and microlite crystallization during pre-climactic events of the 1991 eruption of Mt. Pinatubo, Philippines. Bulletin of Volcanology, 60, 355–380.

Higgins, M.D. (1994) Numerical modeling of crystal shapes in thin sections: estimation of crystal habit and true size. American Mineralogist, 79, 113–119.

Higgins, M.D. (2000) Measurement of crystal size distributions. American Mineralogist, 85, 1105–1116.

Hubbell, J.H., and Seltzer, S.M. (2004) Tables of X-Ray Mass Attenuation Coefficients and Mass Energy-Absorption Coefficients (ver. 1.4) [Online]. Available: http://physics.nist.gov/xaamdi [accessed 2020, April 21]. National Institute of Standards and Technology, Gaithersburg, Maryland.

Jaupart, C., and Allègre, C.J. (1991) Gas content, eruption rate and instabilities of eruption regime in silicic volcanoes. Earth and Planetary Science Letters, 102, 413–429.

Jerram, D.A., and Higgins, M.D. (2007) 3D analysis of rock textures: quantifying igneous microstructures. Elements, 3, 239–245.

Jerram, D.A., Mock, A., Davis, G.R., Field, M., and Brown, R.J. (2009) 3D crystal size distributions: A case study on quantifying olivine populations in kimberlites. Lithos, 112, 223–235.

Jerram, D.A., Dobson, K.J., Morgan, D.J., and Pankhurst, M.J. (2018) The petrogenesis of magmatic systems: Using igneous textures to understand magmatic processes. In S. Burchardt, Ed., Volcanic and Igneous Plumbing Systems, p. 191–229. Elsevier.

Kato, K., and Yamasato, H. (2013) The 2011 eruptive activity of Shinmoedake volcano, Kirishimayama, Kyushu, Japan—overview of activity and volcanic alert level of the Japan meteorological agency—. Earth, Planets and Space, 65, 489–504.

Koch, B., and MacGillavry, C.H. (1962) X-ray Absorption. In C.H. MacGillavry and G.D. Rieck, Eds., International Tables for X-ray Crystallography, Vol. III, p. 157–160. The Kynoch Press, Birmingham, England.

Kouchi, A., Sugawara, Y., Kashima, K., and Sunagawa, I. (1983) Laboratory growth of sector zoned clinopyroxenes in the system CaMgSi2O6-CaTiAl2O6. Contributions to Mineralogy and Petrology, 83, 177–184.

Kozono, T., Ueda, H., Ozawa, T., Koyaguchi, T., Fujita, E., Tomiya, A., and Suzuki, Y.J. (2013) Magma discharge variations during the 2011 eruptions of Shinmoe-dake volcano, Japan, revealed by geodetic and satellite observations. Bulletin of volcanology, 75, 695.

Marsh, B.D. (1988) Crystal size distribution (CSD) in rocks and the kinetics and dynamics of crystallization I: Theory. Contributions to Mineralogy and Petrology, 99, 277–291.

Marsh, B.D. (1998) On the interpretation of crystal size distributions in magmatic systems. Journal of Petrology, 39, 553–599.

Masotta, M., Pontesilli, A., Mollo, S., Armienti, P., Ubide, T., Nazzari, M., and Scarlato, P. (2020) The role of undercooling during clinopyroxene growth in trachybasaltic magmas: Insights on magma decompression and cooling at Mt. Etna volcano. Geochimica et Cosmochimica Acta, 268, 258–276.

Matsumoto, M., Tsuchiyama, A., Nakato, A., Matsuno, J., Miyake, A., Kataoka, A., Ito, M., Tomioka, N., Kodama, Y., Uesugi, K., Takeuchi, A., Nakano, T., and Vaccaro, E. (2019) Discovery of fossil asteroidal ice in primitive meteorite Acfer 094. Science Advances, 5, eaax5078.

Miyabuchi, Y., Hanada, D., Niimi, H., and Kobayashi, T. (2013) Stratigraphy, grain-size and component characteristics of the 2011 Shinmoedake eruption deposits, Kirishima Volcano, Japan. Journal of Volcanology and Geothermal Research, 258, 31–46.

Miyake, A., Matsuno, J., and Toh, S. (2014) Sample preparation toward seamless 3D imaging technique from micrometer to nanometer scale. Microscopy, 63, i24–i25.

Mock, A., and Jerram, D.A. (2005) Crystal size distributions (CSD) in three dimensions: insights from the 3D reconstruction of a highly porphyritic rhyolite. Journal of Petrology, 46, 1525–1541.

Morgan, D.J., and Jerram, D.A. (2006) On estimating crystal shape for crystal size distribution analysis. Journal of Volcanology and Geothermal Research, 154, 1–7.

Muir, D.D., Blundy, J.D., and Rust, A.C. (2012) Multiphase petrography of volcanic rocks using element maps: a method applied to Mount St. Helens, 1980–2005. Bulletin of volcanology, 74, 1101–1120.

Mujin, M., and Nakamura, M. (2014) A nanolite record of eruption style transition. Geology, 42, 661–614.

Mujin, M., and Nakamura, M. (2020) Late-stage groundmass differentiation as a record of magma stagnation, fragmentation, and rewelding. Bulletin of Volcanology, 82. https://doi.org/10.1007/s00445-020-01389-1

Mujin, M., Nakamura, M., and Miyake, A. (2017) Eruption style and crystal size distributions: Crystallization of groundmass nanolites in the 2011 Shinmoedake eruption. American Mineralogist, 102, 2367–2380.

Nakada, S., Nagai, M., Kaneko, T., Suzuki, Y., and Maeno, F. (2013) The outline of the 2011 eruption at Shinmoe-dake (Kirishima), Japan. Earth, planets and space, 65, 475–488.

Nakano, T., Nakashima, Y., Nakamura, K., and Ikeda, S. (2000) Observation and analysis of internal structure of rock using X-ray CT. Journal of Geological Society of Japan, 106, 363–378 (in Japanese).

Nakano, T., Tsuchiyama, A., Uesugi, K., Uesugi, M., and Shinohara, K. (2006) "Slice" -Softwares for basic 3-D analysis-. Available: http://www-bl20.spring8.or.jp/slice/. Japan Synchrotron Radiation Research Institute (JASRI), Hyogo.

Peterson, T.D. (1996) A refined technique for measuring crystal size distributions in thin section. Contributions to Mineralogy and Petrology, 124, 395–405.

Preece, K., Barclay, J., Gertisser, R., and Herd, R.A. (2013) Textural and micro-petrological variations in the eruptive products of the 2006 dome-forming eruption of Merapi volcano, Indonesia: implications for sub-surface processes. Journal of Volcanology and Geothermal Research, 261, 98–120.

Shea, T., and Hammer, J.E. (2013) Kinetics of cooling- and decompression-induced crystallization in hydrous mafic-intermediate magmas. Journal of Volcanology and Geothermal research, 260, 127–145.

Shoji, T. (2002) Drawing of a Wulff Net and Stereographic Projection by MS-Excel/VBA. Geoinformatics, 13, 3–8 (in Japanese).

Suzuki, Y., Yasuda, A., Hokanishi, N., Kaneko, T., Nakada, S., and Fujii, T. (2013) Syneruptive deep magma transfer and shallow magma remobilization during the 2011 eruption of Shinmoe-dake, Japan—Constraints from melt inclusions and phase equilibria experiments. Journal of Volcanology and Geothermal Research, 257, 184–204.

Suzuki, Y., Maeno, F., Nagai, M., Shibutani, H., Shimizu, S., and Nakada, S. (2018) Conduit processes during the climactic phase of the Shinmoe-dake 2011 eruption (Japan): Insights into intermittent explosive activity and transition in eruption style of andesitic magma. Journal of Volcanology and Geothermal Research, 358, 87–104.

Taddeucci, J., Pompilio, M., and Scarlato, P. (2004) Conduit processes during the July–August 2001 explosive activity of Mt. Etna (Italy): inferences from glass chemistry and crystal size distribution of ash particles. Journal of Volcanology and Geothermal Research, 137, 33–54.

Takeuchi, A., Uesugi, K., and Suzuki, Y. (2009) Zernike phase-contrast x-ray microscope with pseudo-Kohler illumination generated by sectored (polygon) condenser plate. Journal of Physics: Conference Series, 186, 012020.

Tanaka, R., and Hashimoto, T. (2013) Transition in eruption style during the 2011 eruption of Shinmoe-dake, in the Kirishima volcanic group: Implications from a steady conduit flow model. Earth, Planets and Space, 65, 645–655.

Tsuchiyama, A., Uesugi, M., Matsushima, T., Michikami, T., Kadono, T., Nakamura, T., Uesugi, K., Nakano, T., Sandford, S.A., Noguchi, R., and others. (2011) Three-dimensional structure of Hayabusa samples: origin and evolution of Itokawa regolith. Science, 333, 1125–1128.

Tsuchiyama, A., Nakano, T., Uesugi, K., Uesugi, M., Takeuchi, A., Suzuki, Y., Noguchi, R., Matsumoto, T., Matsuno, J., Nagano, T., and others. (2012) Analytical dual-energy microtomography: A new method for obtaining three-dimensional phase images and its application to Hayabusa samples. Geochimica et Cosmochimica Acta, 116, 5–16.

Ubide, T., and Kamber, B.S. (2018) Volcanic crystals as time capsules of eruption history.

Nature Communications, 9, 326.

Uesugi, K., Takeuchi, A., and Suzuki, Y. (2006) Development of micro-tomography system with Fresnel zone plate optics at SPring-8. In U. Bonse, Ed., Proceedings of SPIE OPTICS + PHOTONICS, 6318, 63181F. International Society for Optics and Photonics, Bellingham, Washington.

Wadsworth, F.B., Llewellin, E.W., Vasseur, J., Gardner, J.E., and Tuffen, H. (2020) Explosive-effusive volcanic eruption transitions caused by sintering. Science Advances, 6, eaba7940.

Witter, M., Furman, T., LaFemina, P., and Feineman, M. (2016) Understanding magmatic processes at Telica volcano, Nicaragua: Crystal size distribution and textural analysis. American Mineralogist, 101, 1052–1060.

Woods, A.W., and Koyaguchi, T. (1994) Transitions between explosive and effusive eruptions of silicic magmas. Nature, 370, 641–644.

Zingg, T. (1935) Beitrag zur Schotteranalyse. Schweizerische Mineralogische und Petrographische Mitteilungen, 15, 39–140 (in German).

Figure captions

Figure 1. Analytical procedures in this study.

The shaded part on the left represents the prevalent procedure to acquire CSDs. In this study, we additionally obtained *S*-plot and *I*-plot SEM-CSDs from the estimated *L*-plot ones, and CT-CSDs and 3D aspect ratios by SR-XCT analyses directly.

Figure 2. Simulation of CSDs for different growth kinetics.

Considering non-steady (**a**) nucleation rates and (**b**) growth rates, we simulate (**c**, **d**) the resultant CSDs based on the equations in Marsh (1998). Detailed descriptions are included in Appendix 2. Gray lines represent slow ascent with low ΔT_{eff}, and black lines represent fast ascent with high ΔT_{eff}. Dashed lines in (**c**) represent the case of relatively constant growth rates, whereas solid lines in (**d**) represent the simulation with the assumption that growth rates increase significantly with ΔT_{eff}. Because dashed and solid lines are representative of *S*-plot and *L*-plot CSDs, respectively, the values of G_o and *b* for the solid lines are set higher than those for the dashed lines.

Figure 3. Backscattered electron (BSE) images of the groundmass of pumice clasts from

the 2011 Shinmoedake eruption. (**a**) The gray pumice from the sub-Plinian eruption. (**b**) The gray pumice from the Vulcanian explosion. Groundmass crystal phases are Fe-Ti oxides, pyroxene, and plagioclase (in order of decreasing brightness). The brightness of the groundmass glass is similar to that of plagioclase. The regions shown here were included in the area analyzed for acquisition of the SEM-CSDs. Abbreviations: Pl, plagioclase; Px, pyroxene; Ox, Fe-Ti oxides.

Figure 4. (**a**) CT images and (**b**) orientations of pyroxene long axes (*L*). (**a**) Representative CT images of the four CT specimens. The image of Vul_2 was denoised using the iterative nonlocal means filter (Bruns et al. 2017). Abbreviations: Pl, plagioclase; Px, pyroxene; Ox, Fe-Ti oxides; Gl, glass. (**b**) Pole figures showing the elongation directions of groundmass pyroxenes in each CT specimen. Crystals smaller than 5 pixels in short-axis length (*S*) were excluded. The orientations of the pyroxenes were constrained by plagioclase microlites and vesicles, but no lineation was observed. The pole figures were drawn using the program *VBAWulff* (Shoji 2002).

Figure 5. 3D reconstructions of groundmass pyroxene crystals. (**a**, **b**) The sub-Plinian

pumice (specimen sP_1), and (**c**, **d**) the Vulcanian pumice (Vul_2). Only crystals included in the CT-CSDs are shown; crystals truncated by the edge of the specimen are excluded. Crystals exhibit swallowtail textures in the sub-Plinian pumice (**b**), but have flat ends in the Vulcanian pumice (**d**).

Figure 6. 3D shape variations of groundmass pyroxenes. (**a**) Zingg diagram (Zingg, 1935) of the 3D shape distribution in both pumice samples. Stars indicate the average 3D shape in each pumice. Most crystals are acicular, though their shapes vary widely. (**b**) Elongation (L/S) vs. crystal short-axis size (S). We were unable to measure crystals longer than $25\sqrt{3}$ µm owing to the restricted size of the CT specimens (dark shaded area at upper right). The dotted lines indicate contours of specific long-axis lengths (L). Note that crystals with $S < 5$ pixels were excluded from both (**a**) and (**b**).

Figure 7. Histograms of the L/S aspect ratios of groundmass pyroxenes in (**a**) the sub-Plinian pumice and (**b**) the Vulcanian pumice. The dashed lines indicate the representative values estimated from 2D SEM images by *CSDslice* (i.e., L'_{2D}/S'_{2D}).

Figure 8. CT-CSDs plotted based on different size criteria. The 3D CSDs of groundmass pyroxenes were calculated from XCT measurements of (**a**) short-axis length (S), (**b**) intermediate-axis length (I), and (**c**) long-axis length (L). Gray symbols represent size intervals that include crystals smaller than 5 pixels in length. Regression lines are not shown for the downturned parts of the distributions at the smallest size fractions.

Figure 9. Distributions of crystal cross-sectional aspect ratios (w/l) from SEM measurements and simulations by *CSDslice*. (**a**) The sub-Plinian pumice, and (**b**) the Vulcanian pumice. Distributions of w/l measured from the SEM images are shown in gray. Solid lines indicate distributions for the 3D aspect ratios estimated from the 2D data by *CSDslice* (i.e., S'_{2D} : I'_{2D}: L'_{2D} = 1.0 : 1.4 : 2.3 for the sub-Plinian pumice and 1.0 : 1.1 : 4.5 for the Vulcanian one). Dashed lines represent the distributions simulated for the 3D aspect ratios of the crystal shapes in the *CSDslice* database (1.0 : 1.4 : 9.0 and 1.0 : 1.3 : 5.0) closest to the XCT-averages for the sub-Plinian and Vulcanian pumice samples (1.0 : 1.4 : 9.4 and 1.0 : 1.3 : 5.1, respectively).

Figure 10. SEM-CSDs of groundmass pyroxene crystals in the sub-Plinian (‘sP’) and

Vulcanian ('Vul') pumice samples plotted against (**a**) *S*, (**b**) *I*, and (**c**) *L*.

Figure 11. Comparison of CT-CSDs and SEM-CSDs for (**a**–**c**) the sub-Plinian pumice and (**d**–**f**) the Vulcanian pumice. The SEM-CSDs are the same as those in Figure 10, and the CT-CSDs are shown in black. Gray symbols in the CT-CSDs indicate size intervals including crystals smaller than 5 pixels in length.

Figure 12. Difference in CSDs between the sub-Plinian and Vulcanian pumice samples. CT-CSDs (solid lines) and SEM(*w*)-CSDs (dashed lines) are shown as (**a**) *L* plot and (**b**) *S* plot. Note that the SEM(*w*)-CSDs in this figure were corrected with the XCT average 3D aspect ratio instead of the 2D-estimated value. The enlarged view of CSDs in small size range is shown at the upper right in each panel.

Figure S1. Effect of 3D aspect ratio on SEM(*w*)-CSDs. The sub-Plinian SEM(*w*)-CSDs corrected with various 3D shapes are shown as (**a**) *L* plots and (**b**) *S* plots. (**a**) The shapes of *L*-plot CSDs significantly depend on the 3D aspect ratio, whereas (**b**) *S*-plot CSDs preserve almost the same shape with vertical displacement due to the ratio.

Figure S2. Comparison of CT-CSDs, SEM(2D)-CSDs, and SEM(3D)-CSDs for (**a**–**c**) the sub-Plinian pumice and (**d**–**f**) the Vulcanian pumice. The leftmost panels (**a**, **d**) are plotted against *S*, the center panels (**b**, **e**) against *I*, and the rightmost panels (**c**, **f**) against *L*. The CT-CSDs (black) include gray symbols indicating size intervals including crystals smaller than 5 pixels in length.

Figure S3. Differences in SEM-CSDs according to eruption style and plot type. SEM(2D)-CSDs and SEM(3D)-CSDs are shown in the upper (**a**–**c**) and lower rows (**d**–**f**), respectively. In each panel, the CSDs of the sub-Plinian pumice ('sP') are shown in black, and those of the Vulcanian pumice ('Vul') in gray. In the *L* plot (**c**, **f**), solid and dotted lines represent SEM(*w*)-CSDs and SEM(*l*)-CSDs, respectively.

Appendix

1. Aspect ratio dependence of SEM-CSDs

CSDCorrections (Higgins 2000) addresses two stereological problems of the conversion from 2D to 3D: the cut-section effect and the intersection-probability effect. The stereological corrections are applied sequentially from the largest size interval (i.e., the first interval) to smaller intervals. The number of crystals per unit volume in the *i*th interval, n_{Vi}, is converted stereologically from the number of crystal cross sections per unit area, n_{Ai}, as (modified from Equations 5 and 8 of Higgins 2000 and Equation 7 of Sahagian and Proussevitch 1998):

$$n_{Vi} = \left(n_{Ai} - \sum_{j=1}^{i-1} n_{Vj} P_{ji} \overline{H}_j \right) \cdot \frac{1}{P_{ii} \overline{H}_i} = n_{Ai} \cdot \frac{1 - \sum_{j=1}^{i-1} \frac{n_{Vj} P_{ji} \overline{H}_j}{n_{Ai}}}{P_{ii}} \cdot \frac{1}{\overline{H}_i}$$

$$n_{Vi} = n_{Ai} \cdot \frac{1 - CF_i}{P_{ii}} \cdot \frac{\ln(y_i/x_i)}{y_i(L) - x_i(L)} \quad \text{(A1)}$$

where $x_i(L)$ and $y_i(L)$ are the lower and upper limits of the *i*th interval of L, P_{ji} is the probability that a crystal with a true (i.e., determined in 3D) size in the *j*th interval will have a cross-sectional length in the *i*th interval, and CF_i is a correction factor representing the proportion of crystals with true sizes larger than the *i*th interval among the cross sections within that interval. $-H_i$ {note to typesetting, this minus sign is the overbar on top of the *H*} is the Mean Projected Height defined by Tuffen (1998) and the Equation 8 of Higgins (2000). Regarding the Equation (A1), the first term, n_{Ai}, is obtained by dividing the number of crystal cross sections by the area analyzed. The second and third terms are correction terms for the effects of sectioning and the probability of intersection, respectively. Note that the interval width as a function of *L* is calculated from Equation (1). More specifically, in the case of conversion from *w*, the interval width is:

$$y_i(L) - x_i(L) = A \cdot \left(y_i(S) - x_i(S)\right) \quad \text{(A2a)}$$

and in the case of conversion from *l*, it is:

$$y_i(L) - x_i(L) = B \cdot \left(y_i(I) - x_i(I)\right). \quad \text{(A2b)}$$

The population density in the *i*th interval, N_i, is obtained by dividing n_{Vi} (cf. Equation A1) by the interval width (Equation 10 of Higgins 2000). Consequently, *CSDCorrections* calculates the *L*-plot population density as:

$$N_i(L) = \frac{n_{Vi}}{y_i(L)-x_i(L)} = n_{Ai} \cdot \frac{1-CF_i}{P_{ii}} \cdot \frac{\ln(y_i/x_i)}{\left(y_i(L)-x_i(L)\right)^2}$$

$$N_i(L) = \frac{1}{A^2} \cdot \frac{1-CF_i}{P_{ii}} \cdot \frac{n_{Ai}\ln(y_i/x_i)}{\left(y_i(S)-x_i(S)\right)^2} \quad \text{(A3a)}$$

or

$$N_i(L) = \frac{1}{B^2} \cdot \frac{1-CF_i}{P_{ii}} \cdot \frac{n_{Ai}\ln(y_i/x_i)}{\left(y_i(I)-x_i(I)\right)^2}. \quad \text{(A3b)}$$

To obtain *S*-plot and *I*-plot CSDs, we converted the *L*-plot population densities output by *CSDCorrections*, $N_i(L)$, as:

$$N_i(S) = \frac{n_{Vi}}{y_i(S)-x_i(S)} = \frac{y_i(L)-x_i(L)}{y_i(S)-x_i(S)} \cdot N_i(L) = A \cdot N_i(L) \quad \text{(A4a)}$$

$$N_i(I) = \frac{n_{Vi}}{y_i(I)-x_i(I)} = \frac{y_i(L)-x_i(L)}{y_i(I)-x_i(I)} \cdot N_i(L) = B \cdot N_i(L). \quad \text{(A4b)}$$

Substituting Equation (A3) into Equation (A4) gives:

$$N_i(S) = \frac{1}{A} \cdot \frac{1-CF_i}{P_{ii}} \cdot \frac{n_{Ai} \ln(y_i/x_i)}{\left(y_i(S)-x_i(S)\right)^2} \qquad \text{(A5a)}$$

$$N_i(I) = \frac{1}{B} \cdot \frac{1-CF_i}{P_{ii}} \cdot \frac{n_{Ai} \ln(y_i/x_i)}{\left(y_i(I)-x_i(I)\right)^2}. \qquad \text{(A5b)}$$

The third terms of Equations (A3) and (A5) are independent from the 3D aspect ratio used for the 2D–3D conversion. As shown by the first right-hand terms of the equations, $N_i(L)$ depends more strongly on the aspect ratio than do $N_i(S)$ and $N_i(I)$. In addition to the aspect ratio dependence of the population densities, the *L*-plot SEM-CSDs require an additional correction in which their horizontal axes are enlarged by *A* or *B* times. This procedure softens the slopes of *L*-plot CSDs by *A* or *B* times those in *S*- or *I*-plot CSDs, respectively. Therefore, *L*-plot CSDs are more strongly changed by the aspect ratio (*A* or *B*) than are *S*- and *I*-plot CSDs (Fig. S1).

2. **Simulation of CSDs based on Marsh (1998)**

Marsh (1998) formulated CSDs in the non-steady closed systems by employing the Johnson-Mehl-Avrami equation for crystallinity related to time-variant nucleation and growth rates. Considering the exponential variations in time of nucleation (*J*) and growth (*G*) rates, their functions are

DOI: https://doi.org/10.2138/am-2022-8039. http://www.minsocam.org/

$$J(x) = J_o \exp(ax) \quad \text{(A6)}$$

$$G(x) = G_o \exp(bx) \quad \text{(A7)}$$

where *a* and *b* are constants, and *x* is the dimensionless time (0–1). The dimensionless time *x* is normalized by the crystallization duration, τ (i.e., $x = t/\tau$). The subscript o for the parameters indicates the initial values (i.e., at time $x = 0$). The final size (i.e., at $x = 1$) of a crystal which nucleated at a certain time *x*, $R(x)$, is expressed as follows (cf. Equation 5 in Marsh 1998).

$$R(x) = \frac{G_o \tau}{b}\{\exp(b) - \exp(bx)\} \quad \text{(A8)}$$

The natural logarithm of population density of crystals which nucleated at the certain time *x*, Ln $N(x)$, is expressed as (modified from Equations 3, 12, and 26 in Marsh 1998):

$$\text{Ln}\, N(x) = \text{Ln}(J_o/G_o) - \frac{4\pi}{3} {G_o}^3 J_o \tau^4 f(x, a, b) + (a - b)x \quad \text{(A9)}$$

where the function $f(x, a, b)$ is defined as the Equation 10 in Marsh (1998):

$$f(x, a, b) = \int_0^x \exp(ax')\left\{\int_{x'}^x \exp(bx)\, \mathrm{d}x\right\}^3 \mathrm{d}x'. \quad \text{(A10)}$$

From the Equations (A8) and (A9), we obtain the simulated CSDs for specified kinetic conditions (a, b, J_o, G_o, and τ) by plotting Ln $N(x)$ against $R(x)$ for $x = [0, 1]$. To investigate the effect of increasing growth rate on CSDs under different ascent paths, we simulated four sets of conditions as shown in Table S1. The ranges of the kinetic parameters (Figs 2c and 2d) are realistic (cf. Marsh 1998; Shea and Hammer 2013).

3. SEM-CSDs converted using XCT average aspect ratios

For the stereological conversions, we used two distinct 3D aspect ratios to assess the effect of the estimation error on the CSD shapes: the value estimated from the 2D data by *CSDslice* (Morgan and Jerram 2006) and the average value determined by SR-XCT (Table 4). Here, we refer to the SEM-CSDs converted from the datasets of *w* and *l* and corrected with the ratio estimated from the 2D data as SEM(*w*-2D)-CSDs and SEM(*l*-2D)-CSDs, respectively, and those corrected with the average ratio from the SR-XCT data as SEM(*w*-3D)-CSDs and SEM(*l*-3D)-CSDs, respectively. In addition to the seven types of CSDs presented in the main text, we thus obtained 11 types of CSDs.

Figure S2 compares CT-CSDs, SEM(2D)-CSDs, and SEM(3D)-CSDs. We observed obvious discrepancies between the SEM(2D)-CSDs and the SEM(3D)-CSDs for the sub-Plinian pumice that resulted from the 3D aspect ratio used. The *S*- and *I*-plot SEM-CSDs are vertically displaced but have similar shapes, and the SEM(3D)-CSDs were closer to (i.e., less vertically displaced from) the CT-CSDs (Figs. S2a and S2b; Table 4). Although the SEM(3D)-CSDs were almost consistent with the *L*-plot CT-CSD, the

SEM(2D)-CSDs were considerably distorted (Fig. S2c). In the Vulcanian *L* plot (Fig. S2f), the slopes of the SEM(*w*)-CSDs differed slightly from that of the CT-CSD, irrespective of the 3D aspect ratio used, whereas the SEM(*l*)-CSDs were similar to the CT-CSD. This discrepancy may reflect the non-equivalence between the *w* and *l* datasets (Higgins 1994; Muir et al. 2012), or may indicate that both of the *L*/*S* ratios (*A*) differed from an appropriate value, which is possibly associated with the large variation in the ratios (Castro et al. 2003).

Comparing the sub-Plinian and Vulcanian pumice samples, the SEM(3D)-CSDs were similar in the *L* plot (Fig. S3f), but different in the *S* and *I* plots, especially at the size range of nanolites (Figs. S3d and S3e). Consequently, the SEM(3D)-CSDs more clearly reflected the difference in magma ascent conditions in the *S* and *I* plots than in the *L* plot (Table 4), consistent with the CT-CSDs (Fig. 8).

REFERENCES

Castro, J.M., Cashman, K.V., and Manga, M. (2003) A technique for measuring 3D crystal-size distributions of prismatic microlites in obsidian. American Mineralogist, 88, 1230–1240.

Higgins, M.D. (1994) Numerical modeling of crystal shapes in thin sections: estimation of crystal habit and true size. American Mineralogist, 79, 113–119.

Higgins, M.D. (2000) Measurement of crystal size distributions. American Mineralogist, 85, 1105–1116.

Marsh, B.D. (1998) On the interpretation of crystal size distributions in magmatic systems. Journal of Petrology, 39, 553–599.

Morgan, D.J., and Jerram, D.A. (2006) On estimating crystal shape for crystal size distribution analysis. Journal of Volcanology and Geothermal Research, 154, 1–7.

Muir, D.D., Blundy, J.D., and Rust, A.C. (2012) Multiphase petrography of volcanic rocks using element maps: a method applied to Mount St. Helens, 1980–2005. Bulletin of volcanology, 74, 1101–1120.

Sahagian, D.L., and Proussevitch, A.A. (1998) 3D particle size distributions from 2D observations: stereology for natural applications. Journal of Volcanology and Geothermal Research, 84, 173–196.

Shea, T., and Hammer, J.E. (2013) Kinetics of cooling- and decompression-induced crystallization in hydrous mafic-intermediate magmas. Journal of Volcanology and Geothermal research, 260, 127–145.

Tuffen, H. (1998) L'origine des cristaux dans le chambre magmatique de Santorin (Grèce), p. 45. Université Blaise-Pascal, Clermont-Ferrand, France (not seen; extracted from American Mineralogist, 85, 1112, 2000).

Table 1. Average chemical compositions of groundmass glasses.

	sub-Plinian (wt%)	Vulcanian (wt%)
SiO_2	67.61 (41)	71.99 (21)
TiO_2	0.89 (6)	0.74 (5)
Al_2O_3	14.21 (26)	12.72 (9)
FeO	5.77 (26)	4.26 (13)
MnO	0.11 (5)	0.09 (5)
MgO	1.13 (9)	0.64 (4)
CaO	3.93 (19)	2.57 (9)
Na_2O	3.04 (9)	2.95 (12)
K_2O	3.21 (9)	3.88 (5)
P_2O_5	0.11 (5)	0.16 (5)
Total	100	100

Notes: Each sample was analyzed over 50 distinct regions.

Oxide concentrations were recalculated to total 100% by cation balance.

Table 2. SR-XCT analytical conditions.

Eruptive style	CT specimen	Volume [a] (μm^3)	pixel size (nm)	Number of crystals: for aspect ratio [b]	Number of crystals: for CSD [c]
sub-Plinian	sP_1	6797	40.00	74	83
	sP_2	17,614	24.70	103	103
Vulcanian	Vul_1	8073	33.86	47	48
	Vul_2	15,223	34.70	86	86

[a] Excluding vesicles.

[b] Crystals with S < 5 pixels were excluded.

[c] Crystals smaller than 5 pixels were included.

Table 3. Parameters used in *CSDCorrections* .

Eruptive style	Analyzed area, excluding vesicles		Number of analyzed crystals	3D aspect ratio	Round ness	Size scale length
	(μm^2)	(vesicle%) [a]		$S'_{2D} : I'_{2D} : L'_{2D}$ (XCT average)		Number of bins per decade [b]
sub-Plinian	20,077	57.3	793	1.0 : 1.4 : 2.3 (1.0 : 1.4 : 9.4)	0.8	5
Vulcanian	19,791	54.5	381	1.0 : 1.1 : 4.5 (1.0 : 1.3 : 5.1)	0.8	5

[a] The percentage of vesicles in the analyzed rectangular area.

[b] Logarithmic base-10 size scale.

Table 4. Results of XCT and SEM analyses.

Eruptive style	3D aspect ratio							S			
	XCT average			2D estimate by *CSDslice*				CT			SE
	S	*I*	*L*	S'_{2D}	I'_{2D}	L'_{2D}	R^2	Slope	Intercept	R^2	Slope
sub-Plinian	1.0	1.4 (6)	9.4 (56)	1.0	1.4	2.3	0.842	-3656	24.8	0.997	-3685
Vulcanian	1.0	1.3 (4)	5.1 (39)	1.0	1.1	4.5	0.662	-2237	23.9	0.997	-2096
ratio (sP/Vul)								1.63			1.76

[a] The size ranges used to calculate regression lines correspond largely to those of CT-CSDs (Fig. 8). The unit of

[b] The SEM-CSDs which were corrected with the average 3D aspect ratio from the XCT data.

[c] The SEM-CSDs which were corrected with the 3D aspect ratio estimated from the 2D data.

[d] The exceptionally deviated part (L < 3 μm; Fig. 11) is included.

[e] Estimates from the datasets of cross-sectional widths or lengths using the XCT average 3D aspect ratios.

-plot CSDs										
EM(*w*-3D) [b]		SEM(*w*-2D) [c]			CT			SEM(*l*-3D) [b]		
Intercept	R^2	Slope	Intercept	R^2	Slope	Intercept	R^2	Slope	Intercept	R^2
25.6	0.994	-3611	26.9	0.991	-2697	24.5	0.997	-2044	24.4	0.996
24.3	0.957	-2004	24.1	0.938	-1426	23.2	0.98	-1230	23.1	0.996
		1.80			1.89			1.66		

Above the fourth and fifth groups of columns: *I*-plot CSDs

slope is mm $^{-5}$.

Regression line of CSD [a]											
									L-plot CSDs		
SEM(*l*-2D) [c]			CT			SEM(*w*-3D) [b]			SEM(*l*-3D) [b]		
Slope	Intercept	R^2	Slope	Intercept	R^2	Slope	Intercept	R^2	Slope	Intercept	R^2
-1983	25.6	0.993	-372	22.3	0.998	-392	23.4	0.994	-304	22.5	0.996
-1226	23.1	0.995	-277	21.3	0.993	-391	22.6	0.981	-314	21.7	0.996
1.62			1.34			1.00			0.97		

						Number density per unit volume (mm^{-3}		
SEM(w-2D) [c]			SEM(l-2D) [c]			XCT	*CSDCorrections* [e]	
Slope	Intercept	R^2	Slope	Intercept	R^2		w	l
-817 [d]	24.5 [d]	0.913	-662 [d]	23.9 [d]	0.959	7.62×10^6	1.85×10^7	9.99×10^6
-441	22.8	0.981	-300	21.6	0.995	5.75×10^6	9.03×10^6	5.25×10^6
1.85 [d]			2.21 [d]					

Figure 1

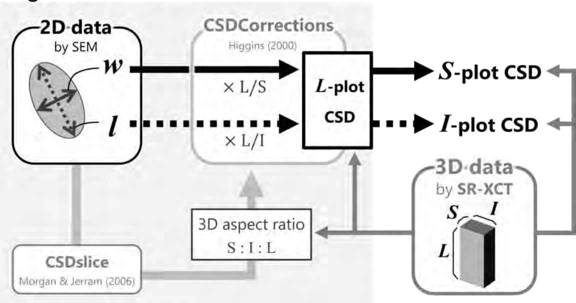

2D-data
by SEM
w
l
CSDCorrections
Higgins (2000)
× L/S
× L/I
L-plot
CSD
S-plot CSD
I-plot CSD
3D-data
by SR-XCT
S
I
L
3D aspect ratio
S : I : L
CSDslice
Morgan & Jerram (2006)

Figure 2

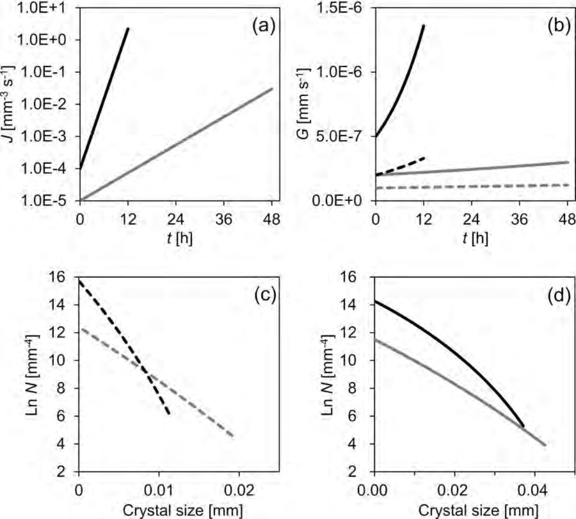
(a)
J [mm-3 s-1]
1.0E+1
1.0E+0
1.0E-1
1.0E-2
1.0E-3
1.0E-4
1.0E-5
0
12
24
36
48
t [h]
(b)
G [mm s-1]
1.5E-6
1.0E-6
5.0E-7
0.0E+0
0
12
24
36
48
t [h]
(c)
Ln N [mm-4]
16
14
12
10
8
6
4
2
0
0.01
0.02
Crystal size [mm]
(d)
Ln N [mm-4]
16
14
12
10
8
6
4
2
0.00
0.02
0.04
Crystal size [mm]

Figure 3

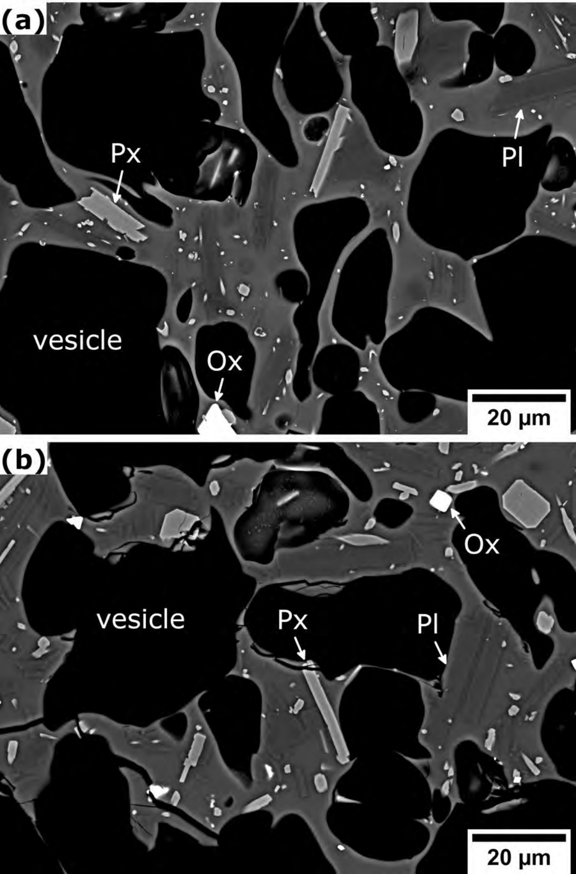

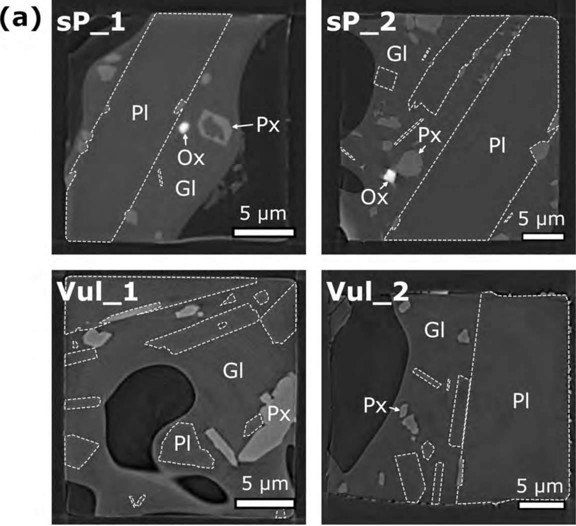
(a)
sP_1
Pl
Px
Ox
Gl
5 μm
sP_2
Gl
Px
Pl
Ox
5 μm
Vul_1
Gl
Px
Pl
5 μm
Vul_2
Gl
Px
Pl
5 μm

Figure 4a

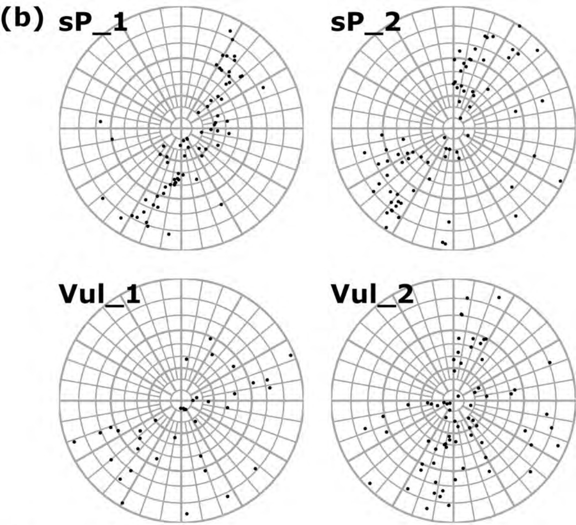

Figure 4b

Figure 5

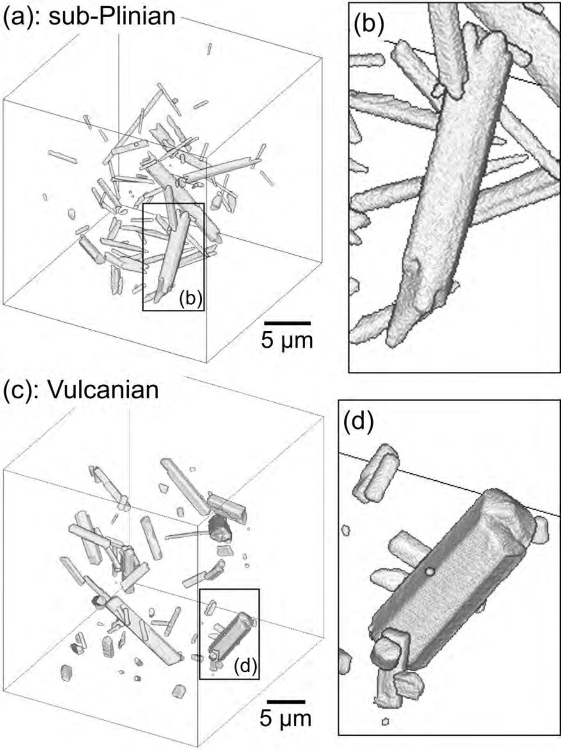

Figure 6a

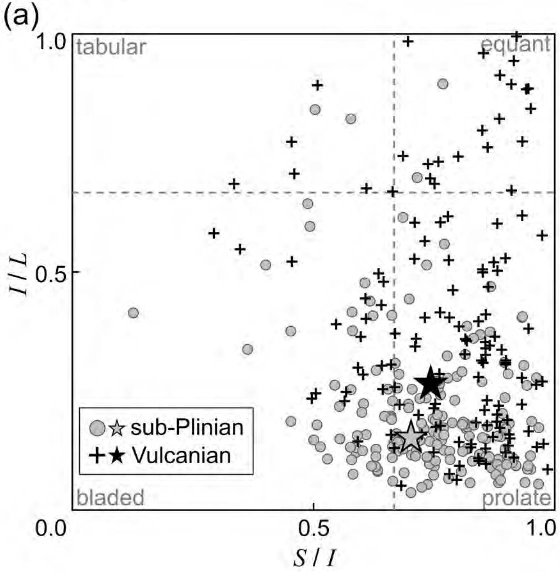
(a)
1.0
0.5
0.0
0.5
1.0
I / L
S / I
tabular
equant
bladed
prolate
sub-Plinian
Vulcanian

Figure 6b

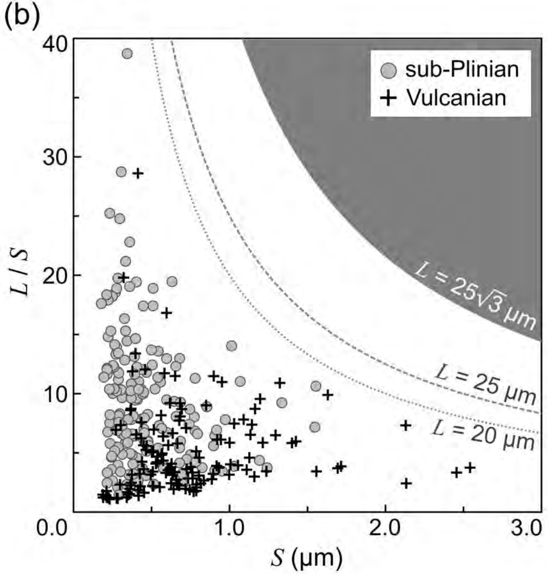

(b)
sub-Plinian
Vulcanian
$L = 25\sqrt{3}$ μm
L = 25 μm
L = 20 μm
L / S
S (μm)
40
30
20
10
0.0
1.0
2.0
3.0

Figure 7

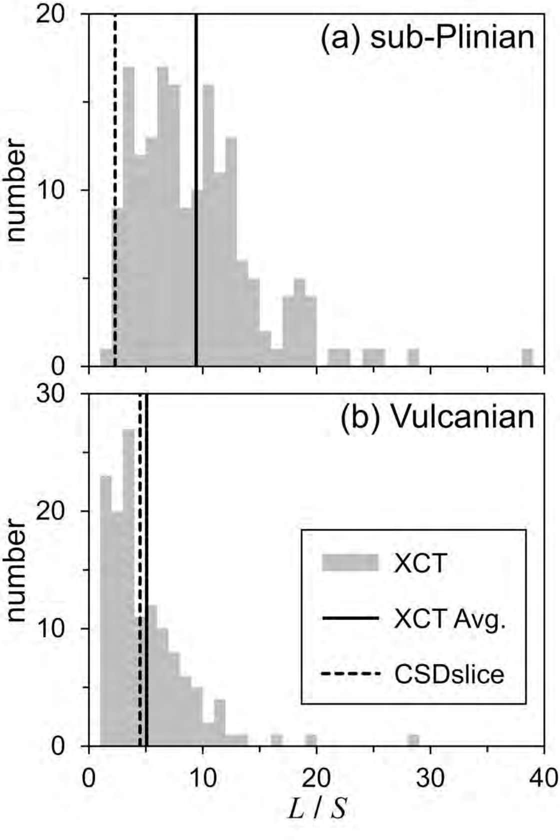

(a) sub-Plinian
(b) Vulcanian
number
number
XCT
XCT Avg.
CSDslice
L / S
0
10
20
0
10
20
30
0
10
20
30
40

Figure 8

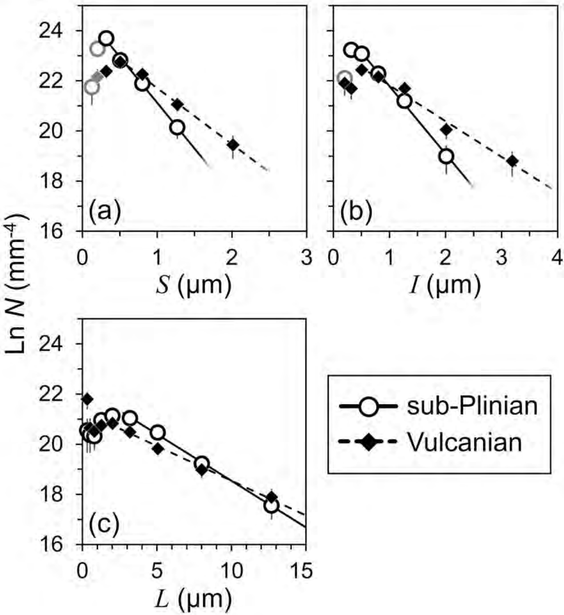

24
22
20
18
16
(a)
0
1
2
3
S (µm)
(b)
0
1
2
3
4
I (µm)
Ln N (mm-4)
24
22
20
18
16
(c)
0
5
10
15
L (µm)
sub-Plinian
Vulcanian

Figure 9

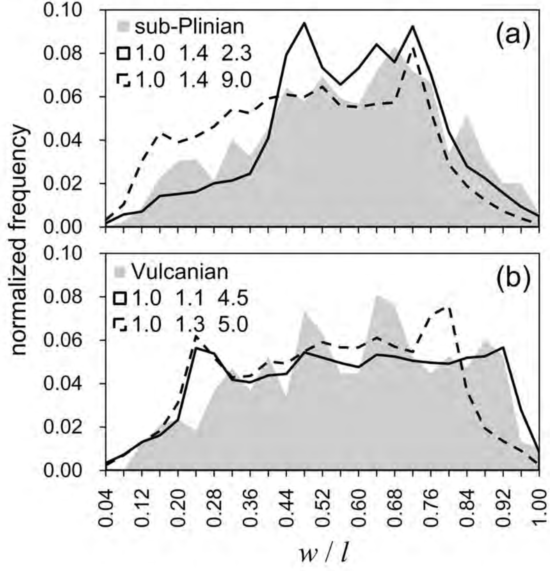
sub-Plinian
(a)
1.0 1.4 2.3
1.0 1.4 9.0
Vulcanian
(b)
1.0 1.1 4.5
1.0 1.3 5.0
normalized frequency
0.10
0.08
0.06
0.04
0.02
0.00
0.04
0.12
0.20
0.28
0.36
0.44
0.52
0.60
0.68
0.76
0.84
0.92
1.00
w / l

Figure 10

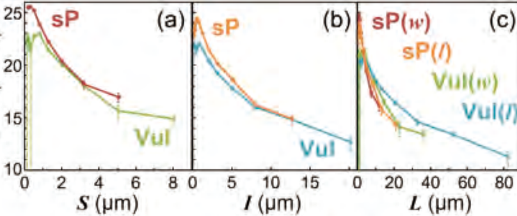

Figure 11

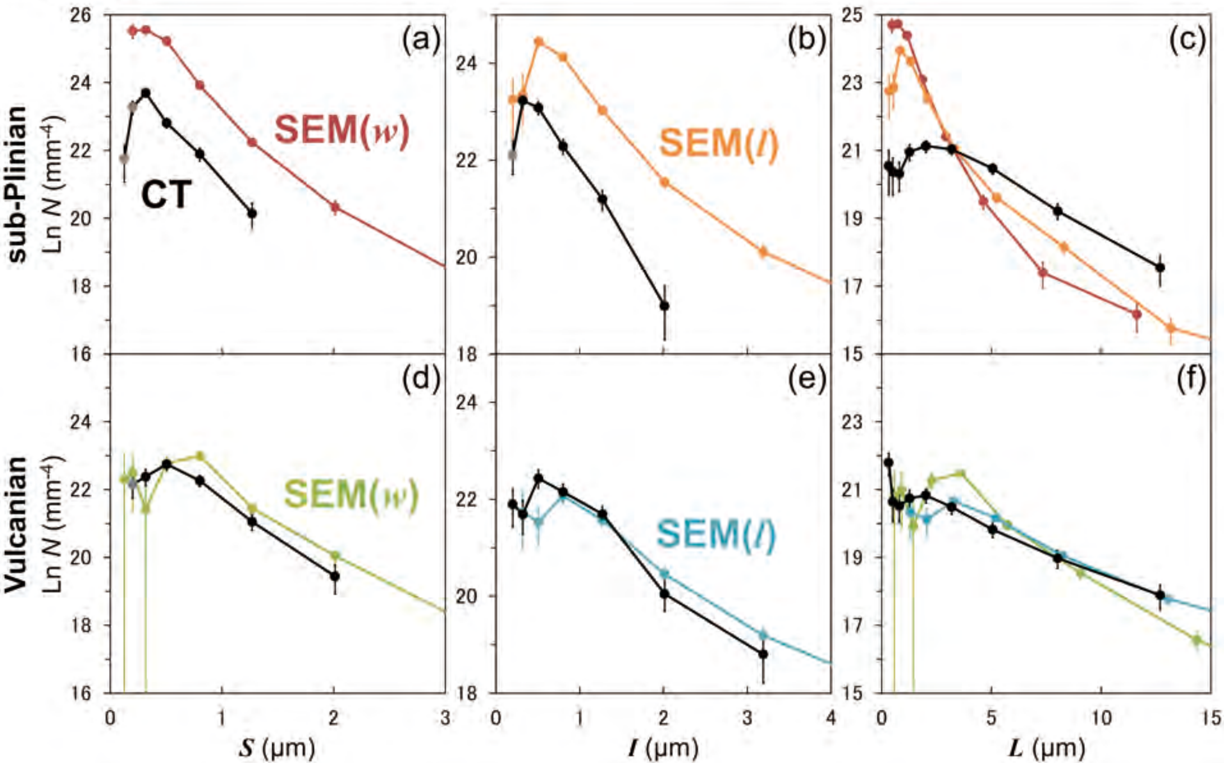

(a)
(b)
(c)
(d)
(e)
(f)
sub-Plinian
Vulcanian
Ln N (mm⁻⁴)
SEM(w)
SEM(l)
CT
S (μm)
I (μm)
L (μm)

Figure 12